PCCP

Accepted Manuscript

ROYAL SOCIETY OF CHEMISTRY

www.rsc.org/pccp

Physical Chemistry Chemical Physics

Orbital Change Manipulation Metal-Insulator Transition Temperature in W Doping VO_2

Xinfeng He[a], Yijie Zeng[a], Xiaofeng Xu*[a], Congcong Gu[a]， Fei Chen[a], Binhe Wu[a] , Chunrui Wang[a], Huaizhong Xing[a], Xiaoshuang Chen*[b], Junhao Chu [b]

[a]*Department of Applied Physics, Donghua University, No.2999, North Renmin Road, Songjiang District, Shanghai 201620, P.R. China*

[b]*National Laboratory for Infrared Physics, Chinese Academy of Sciences, Shanghai Institute of Technical Physics, No.500 Yutian Road, Shanghai 200083, P.R. China*

*Corresponding author. E-mail: xxf@dhu.edu.cn or xschen@mail.sitp.ac.cn

Abstract

Series of epitaxial $V_{1-x}W_xO_2$ ($0 \le x \le 0.76\%$) nanocrystalline films on c-plane sapphire substrates have been successfully synthesized. Orbital structures of $V_{1-x}W_xO_2$ films with monoclinic and rutile states have been investigated by ultraviolet-infrared spectra combined with first principle calculations. Experimental and calculated results show that the overlaps of π^* and $d_{//}$ orbital increase with increasing W doping content for rutile state. Meanwhile, for monoclinic state, the optical band gap decreases from 0.65 to 0.54 eV with increasing W doping concentration. Clear evidence is found that the $V_{1-x}W_xO_2$ thin film phase transition temperature change comes from orbital structure variations. It shows that, with increasing W doping concentration, the decrease of rutile $d_{//}$ orbital occupancy can reduce the strength of V-V interactions, which finally

results in phase transition temperature decrease. The experiment results reveal that the $d_{//}$ orbital is very important for VO_2 phase transition process. Our findings open a possibility to tune VO_2 phase transition temperature through the orbital engineering.

1. INTRODUCTION

Vanadium dioxide (VO_2), which can exhibit a dramatic metal-insulator transition (MIT), has been investigated extensively for decades[1,2]. The phase transition is accompanied by a simultaneous structural distortion from a high-temperature metallic state with a rutile structure to a low-temperature insulating state with a monoclinic structure[3]. As its great technological potential and intriguing physical properties[4,5,6], this material has been used by many modern electronics devices[7], optical switches[8], in particular for so-called smart windows[9]. Although many experimental and theoretical investigations have been performed, there are many unresolved puzzles about VO_2 MIT mechanism[10,11,12]. Recently, many studies have attempted to modify VO_2 phase transition, especially lowering its transition temperature[11, 12, 13,14].

Generally, the phase transition temperature of VO_2 can be manipulated by doping or strain. In order to control the properties of VO_2, it is essential to identify the effects of doping and strain on its phase transition process[11,13,14]. For instance, it has been reported that VO_2 doped with tungsten (W), molybdenum (Mo) and magnesium (Mg) can lower the transition temperature T_{MIT}. This provides various ways for tailoring VO_2 phase transition temperature T_{MIT}[15,16,17,18]. Among them, the most effective route for T_{MIT} reduction may be to dope some W atoms[19]. Several experimental investigations have been carried out and attempted to explain the origin of T_{MIT} reduction in W doping VO_2. Based on x-ray absorption fine structure (XAFS) spectrometry, Jamie M et al. show that a significant expansion along certain crystal axes directions occurs during the phase transition process for W doping VO_2[20]. They considered that the biaxial strain on the sublattices around W sites leads to the breaking of bonds between Peierls-paired V ions and lower the transition temperature. Besides, by using synchrotron radiation X-ray absorption spectroscopy combined with first-principles calculations, it has been considered that the symmetric W core drives the twisting of the monoclinic VO_2 lattice to form rutile phase VO_2[21]. However, these studies are limited to atomic structure evolutions and do not exploit the orbital configuration. On the other hand, the chemical substitution of V atoms by W atoms with different atom sizes and valence states inevitably induces potential mismatches and defects in the lattice structure. They produce additional electrons and these electrons are accommodated in the π^* orbital, which can further affect its orbital structures[22]. In fact, the orbital occupancy in transition-metal oxides plays a crucial role[23]. Nagaphani Aetukuri and colleagues has also reported that VO_2 orbital was strongly affected by the interfacial strain[11]. They show that the strain-induced orbital occupancy changes can tune the transition temperature of VO_2 by varying the thickness of the RuO_2 buffer layer. As a result, in spite of great efforts to understand MIT in W doping VO_2, the nature of lowering phase transition temperature remains unclear.

In this paper, to explore the mechanism of VO_2 T_{MIT} reduction induced by W doping, we systematically study orbital structures of rutile and monoclinic states of $V_{1-x}W_xO_2$ ($0 \le x \le 0.76\%$) thin films. We demonstrate the orbital changes of $V_{1-x}W_xO_2$ by using a double beam ultraviolet-infrared spectrophotometer with photon energy from 0.5 to 5.0 eV. With the help of first principle calculations, a clear physical picture of T_{MIT} reduction in W doping VO_2 films can be reconstructed. Experimental results indicate that $V_{1-x}W_xO_2$ thin film phase transition temperature T_{MIT} is strongly affected by the $d_{//}$ orbital occupancy, suggesting that the $d_{//}$ orbital can play a critical role during VO_2 phase transition process.

2 EXPERIMENTAL SECTIONS

Nanocrystalline $V_{1-x}W_xO_2$ films with the thickness ~165 nm were grown by the sputtering oxidation coupling method. Samples were prepared on c-plane sapphire substrate and the vacuum chamber was evacuated down to 5×10^{-3}Pa. Under the conditions of 1.0 Pa and 45 W in pure Ar, the metallic vanadium mixtured with WO_3 was deposited on the substrate at room temperature. The diameter of target was 60 mm. The distance between target and substrate was fixed at 120 mm. The substrate was rotated at 13 rpm to ensure uniformity of film deposition. In order to eliminate contamination on the target surface, pre-sputtering of the vanadium metal and WO_3 targets were performed before depositing the metallic vanadium mixture with WO_3 thin film. After deposition, the mixture film was taken out from the chamber, and then put in a rapid annealing furnace for further oxidation. A more detailed preparation of thin films has been described elsewhere[24].

The structural characteristics of samples were analyzed by X-ray diffraction (XRD) on a Bruker D8 Discover system with Cu Kα radiation (λ=1.54055Å) from a generator operating at 40 kV and 40 mA. X-ray photoelectron spectroscopy (XPS) experiments were carried out on a RBD upgraded PHI-5000C ESCA system (PerkinElmer). The Mg Ka radiation (hν = 1253.6 eV) was operated at 14 kV and 20 mA. The carbonaceous C1s line (284.6 eV) was used as reference to calibrate the binding energies. The electrical properties for the heating process were measured through four-point probe method. The samples were placed on a ceramic heater with temperature accuracy of ±0.1℃.

The normal-incident transmittance spectra were recorded at 300 and 375 K using a double beam ultraviolet-infrared spectrophotometer (PerkinElmer Lambda 950) at the photon energy from 0.5 to 5.0 eV (250–2500 nm) with a spectral resolution of 2 nm. We retrieved the optical absorption of the thin films through numerical calculations, taking into consideration the contribution from the substrate of which optical constants was obtained separately at each temperature. The thicknesses of thin films were measured by XP-200 Surface Profiler (Ambios Technology Inc.).

3 RESULTS AND DISCUSSION

3.1 Orbital Structures

Above the transition temperature T_{MIT}, VO_2 belongs to metallic state with a rutile crystal structure, in which vanadium (V) atoms are located at the center of oxygen octahedron, as shown in left of Fig. 1(a). In rutile structure, each VO_6 octahedron shares edges with its two neighboring octahedron, forming chains along the c_r axis. When VO_2 is cooled below the transition temperature T_{MIT}, VO_2 transforms into insulating state with a monoclinic structure, which appears a twisting of V-V pairs due to an antiferroelectric shift of neighboring V atoms[25], shown by the green arrows in the right of Fig. 1(a).

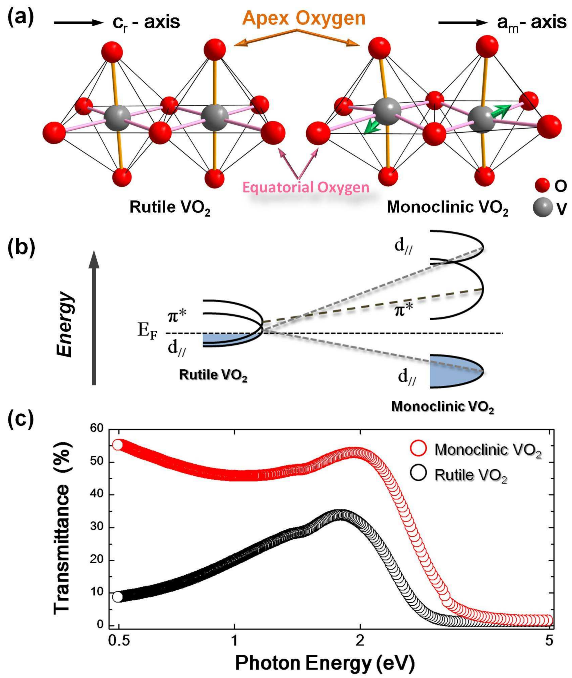

Figure 1. (a) VO_2 crystal structure for rutile and monoclinic states. During the MIT process, the V atoms move directions are marked by the green arrows. (b) Schematic of the orbital change during VO_2 phase transition process. (c) VO_2 transmittance spectra for rutile and monoclinic states, respectively.

Accompanied with VO_2 structure transition, the orbital structures also change (Fig.1(b)) near the Fermi level (E_F)[26]. For rutile state, the $d_{//}$ orbital overlaps with the π^* orbital near E_F makes it exhibit metallic property. For monoclinic state, the twisting of V-V pair causes splitting of the $d_{//}$ orbital into filled bonding and empty antibonding orbital, meanwhile, make the π^* orbital move to a higher energy level. The optical behaviors can directly reflect the orbital structure change during this phase transition process[19,27,28]. For example, the experimental transmittance spectra of VO_2 film for rutile and monoclinic state are shown in Fig. 1(c). It can be observed that transmittance spectra exhibit obvious differences in peak positions and relative intensity with the photon energy from 0.50 to 3.65 eV.

3.2 T_{MIT} Reduction

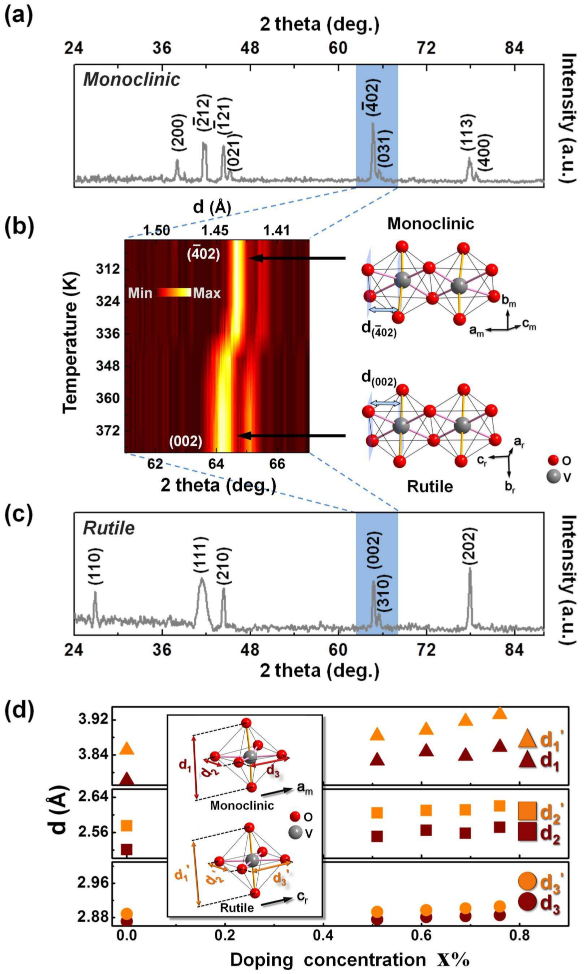

Figure 2. (a) The XRD patterns of $V_{1-x}W_xO_2$ thin film in the monoclinic state with W doping

concentration x=0.00%. (b) *In situ* XRD patterns of $V_{1-x}W_xO_2$ with x=0.00% around the (002) (or ($\bar{4}02$)) peak clearly revealing the structural transition from monoclinic to rutile phases. The right diagrams are schematics of crystal faces ($\bar{4}02$) and (002) marked by blue planes. (c) The XRD patterns of $V_{1-x}W_xO_2$ thin film with x=0.00% in the rutile state. (d) Average bond distances corresponding to different W doping concentration. The inset shows schematics of the bond distances for the monoclinic (d_1, d_2 and d_3) and rutile (d_1', d_2' and d_3') phases.

Fig. 2(a) shows the θ-2θ XRD scans for $V_{1-x}W_xO_2$ thin film with W doping concentration x=0.00% at room temperature (300 K). There are no other vanadium oxide peaks in the XRD spectra (JCPDS: 43-1051). To clearly demonstrate the structural transition from monoclinic to rutile phases, *in situ* XRD patterns of $V_{1-x}W_xO_2$ thin films are also performed. In Fig. 2(b), the selected temperature-dependent *in situ* XRD patterns of $V_{1-x}W_xO_2$ (x=0.00%) with 2θ from 60 to 69° show that the structural transition process can be indicated by (002) peak of the rutile phase emerging from the monoclinic phase ($\bar{4}02$) peak. Its crystal structure from the low-temperature monoclinic phase to the high-temperature rutile phase exhibits a dramatic change along c_r axis direction. The XRD patterns for $V_{1-x}W_xO_2$ (x=0.00%) at the high temperature (380 K) are plotted in Fig. 2(c), in which all the peaks can be indexed to the rutile phase (JCPDS: 73-2362). *In situ* XRD patterns of $V_{1-x}W_xO_2$ thin films with different W doping concentration are used to calculate the lattice parameters by the Bragg's law: $d_{(hkl)} = \lambda/(2\cdot\sin\theta)$, where $d_{(hkl)}$ is the inter-planar spacing of the lattice planes, λ is the X-ray wavelength (λ=1.54055 Å) and θ is the Bragg angle. With the crystal structure properties of Fig. 1(a), the corresponding average bond lengths of the monoclinic (d_1, d_2 and d_3) and rutile (d_1', d_2' and d_3') phases are calculated from the above lattice parameters, which are shown in Fig. 2(d). It can be observed that the average bond lengths increase slightly, which suggests that the lattices expand with increasing W content.

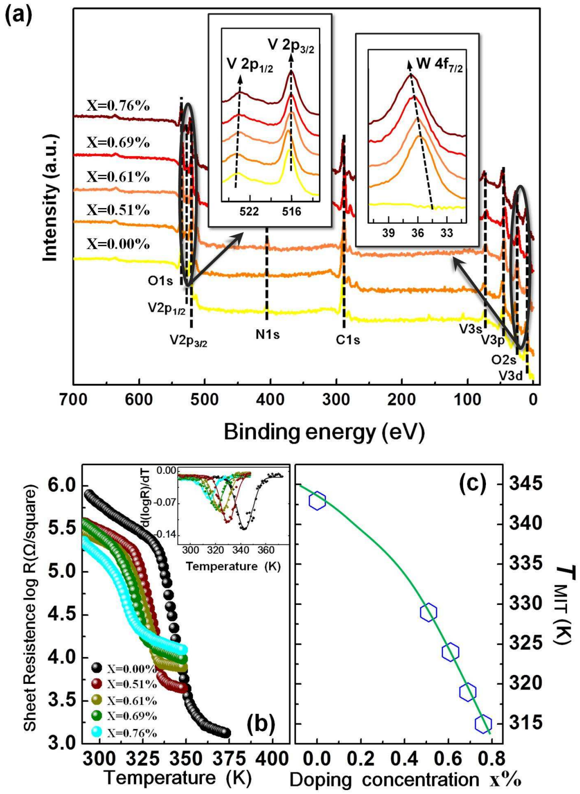

Figure 3. (a) XPS spectrum for $V_{1-x}W_xO_2$ with different W doping concentration. Insets show the high-resolution XPS spectrum of the V $2p_{3/2}$, V $2p_{1/2}$ and W $4f_{7/2}$ edges. (b) Temperature-dependent sheet resistance changes for samples with different W doping concentration. The insets show dlogR/dT versus temperature T curves. (c) The plot of transition temperature T_{MIT} corresponding to different W doping concentration. The line is just guided for eyes.

Fig. 3(a) shows XPS spectra of different $V_{1-x}W_xO_2$ films. The C1s and N1s peaks in all spectra are originated from surface contamination. To get more details, high-resolution XPS spectrums are taken for the binding energies of the core levels V $2p_{3/2}$ and $V2p_{1/2}$ (the left inset of Fig. 3(a)). The C1s signal at 284.6 eV used as binding energies (BE) reference, main fitting peak of $V2p_{3/2}$ is centered at 516.46 eV, which is consistent with binding energy of V^{4+} ion for W doping content x = 0.00 % thin film. With increasing W content x from 0.00 to 0.76%, the V $2p_{3/2}$ and V $2p_{1/2}$ core-level peaks both broaden and shift toward the lower binding energy. The right inset of Fig. 3(a) shows the XPS spectra of the $W4f_{7/2}$ band range[29]. For different amount W, the peaks of W $4f_{7/2}$ shifts toward higher binding energy.

The resistance depending of temperature is shown in Fig. 3(c). Inset in Fig. 3(c) displays standard Gaussian fitting derivative logarithmic plot. The MIT temperatures T_{MIT} of $V_{1-x}W_xO_2$ films are determined by using the temperature-dependent resistance data. Resistance analysis indicates that T_{MIT} significantly reduces from 343 to 315K when W dpping content x increases from 0.00% to 0.76%. The plot of T_{MIT} for different W doping concentration is shown in Fig. 3(d).

3.3 W Doping Effect on Orbital

3.3.1 Spectroscopic Analysis

A three layered structure (air/film/substrate) is constructed to analysis the transmittance spectra of $V_{1-x}W_xO_2$ thin films. The optical constants can be derived by fitting the transmittance spectra using the Drude-Lorentz oscillator model[30,31,32]

$$\tilde{\varepsilon}(E) = \varepsilon_r + i\varepsilon_i = \varepsilon_\infty \left[1 + \sum_{j=1}^{3} \frac{A_j^2}{E_j^2 - E^2 + i\nu E} - \frac{\omega_p^2}{E^2 + i\nu E} \right] \quad (1)$$

where ε_r and ε_i are the real and imaginary part of dielectric function; ε_∞ is the high-frequency dielectric constant; A_j, E_j, υ and E are the center energy, the broadening of the jth oscillator, the damping frequency and the incident photon energy, respectively. ω_p is the plasma frequency. Here, we use the standard theory of electromagnetic plane wave propagation through a stratified medium to calculate the transmittance. Each layer in the structure is modeled by a characteristic complex-valued 2×2 matrix[33,34]. Propagation through a multilayered system can be calculated by the multiplication of the characteristic matrices for each layer. In fitting process, ε_∞, A_j, E_j, υ and ω_p parameters arrive the best approaching experimental values.

3.3.2 Orbital in Rutile Structure

Transmission spectra of rutile state with different W doping concentrations are shown in Fig. 4(a). From Fig. 4(a), it shows that the transmission spectra in the infrared range are enhanced with increasing W doping concentrations. To investigate orbital structure of rutile $V_{1-x}W_xO_2$ near the Fermi level (E_F), the dielectric functions have been calculated in the photon energy range from 0.5 to 5.0 eV by using Eq.(1). For example, the experimental (circle) and fitting (red line) transmittance spectra of $V_{1-x}W_xO_2$ film (x=0.00%) are shown in the inset of Fig. 4(a), respectively. A good agreement is obtained between the experimental and calculated spectra. The optical absorption coefficient (α) is showed in Fig. 4(b). A broad Drude-like tail is observed in the optical absorption regions with the photon energy from 0.5 to 2.0 eV, which is labeled by pink shaded area in Fig. 4(b). The high electron concentration and mobility of rutile $V_{1-x}W_xO_2$ thin films cause Drude dispersion in the infrared regions.

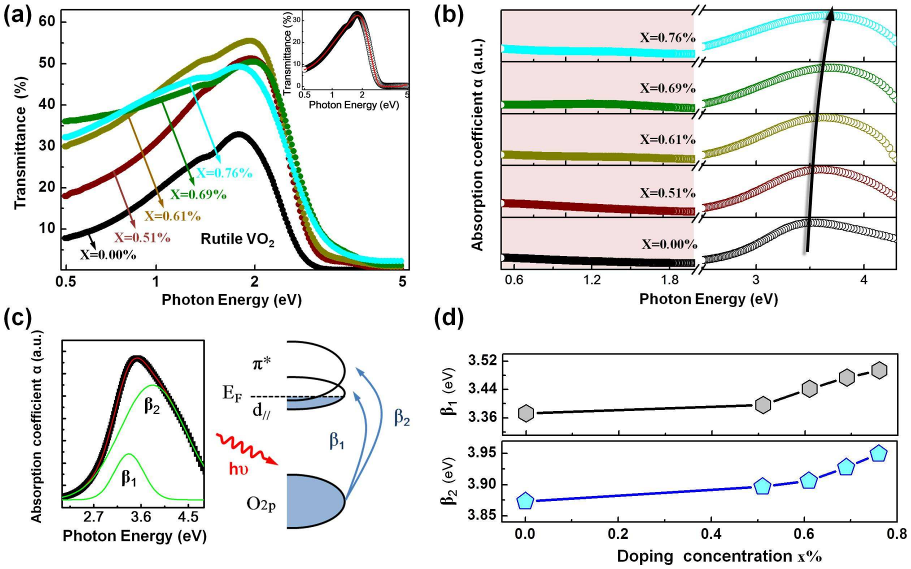

Figure 4. (a) Optical transmittance of $V_{1-x}W_xO_2$ thin films for rutile state. Inset shows a typical experimental (circle) and fitting (red line) transmittance spectra with W doping concentration x=0.00%. (b) The relationship of absorption coefficients and photon energy for $V_{1-x}W_xO_2$ with different W doping concentration. (c) Left: absorption coefficient in the range of 2.0-4.7 eV for $V_{1-x}W_xO_2$ thin film with x =0.61% is used to determine the values of β_1 and β_2; right: schematic electron transition process for β_1 and β_2. (d) The changes of β_1 and β_2 for different W doping concentration.

When the photon energy is in the range of 2.2-5.0 eV, the optical response is ascribed to the different interband electron transitions between filled and empty orbital. For rutile state, it consists two electronic transitions[35,36]: (1) β_1 can be assigned to the transition from non-bonding O 2p orbital to partially filled $d_{//}$ orbital; (2) β_2 is assigned to from O 2p orbital to π* orbital. In the right of Fig. 4(c), the arrows indicate these two transitions across Fermi level. To separate contributions from the different transitions, we performed a classical dispersion analysis. For an example, a typical decomposition of the $V_{1-x}W_xO_2$ thin film with x =0.61% by the Gaussian curve fitting can be seen in the left of Fig. 4(c). For a comparison, all fitting results of β_1 and β_2 for different W doping content are shown in Fig. 4(d). In Fig. 4(d), we find that the $d_{//}$ and π* levels both move to a higher energy level relative to O 2p orbital with increasing W doping concentration.

In Fig. 5(a), we show the relationship of β_2-β_1 and W doping concentration for all samples. Fig. 5(a) displays that β_2-β_1 decreases with increasing W doping concentration. This means that energy level of the π* orbital is lowered relative to that of the $d_{//}$ orbital and the overlap of π*and $d_{//}$ orbital increases with increasing W doping concentration. The orbital energy level changes for rutile state are also schematically shown in Fig. 5(b).

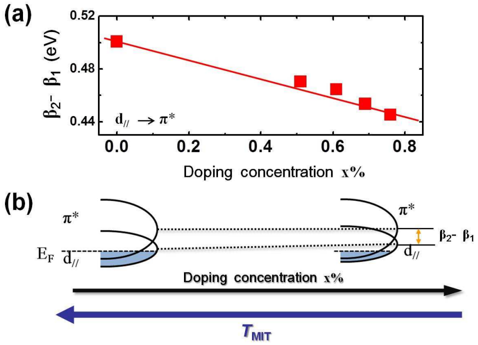

Figurer 5. For rutile state: (a) the relationship of β_2-β_1 and W doping concentration x; (b) schematic of the orbital structure change with increasing W doping concentration.

3.3.3 Orbital in Monoclinic Structure

To comparison，experimental transmission spectra of monoclinic state is shown in Fig. 6(a). Fig. 6(b) shows the absorption coefficient (α), which is calculated from the transmission spectra of Fig. 6(a). To understand orbital structure change, the schematic diagram of orbital structures and electron transitions are summarized in Fig. 6(c). Based on the previous theoretical calculations and experimental observations, the three transition can be uniquely assigned to the followings[35,36]: (1) α_0 corresponds to the optical band gap (OBG), which can be assigned to the indirect transition from the top of filled $d_{//}$ orbital to the bottom of empty π* orbital; (2) α_1 feature can be assigned to the transition from the lower filled $d_{//}$ orbital to the empty π* orbital; (3) α_2 feature is due to the transition from the filled O 2p orbital to empty π* orbital. For example, to obtain detailed orbital information, the left of Fig. 6(c) presents that the indirect OBG is estimated using the power law behavior of Tauc $(\alpha E)^{1/2} \propto (E - Eg)$ for the $V_{1-x}W_xO_2$ thin film with x=0.61%, here α is the absorption coefficient, E is the incident photon energy, and Eg (α_0) is the OBG energy[34]. Besides, the corresponding deconvolution analysis with the photon energy range from 0.5 to5.0 eV is also shown in the middle of Fig. 6(c). As can be seen in Fig. 6(c), three optical transition peaks at absorption spectra are located at 0.616(α_0), 1.27 (α_1) and 3.97(α_2) eV, respectively. Fig. 6(d) shows that the values of α_0, $\alpha_1$and α_2 all shift toward the lower energy level with increasing W doping concentration.

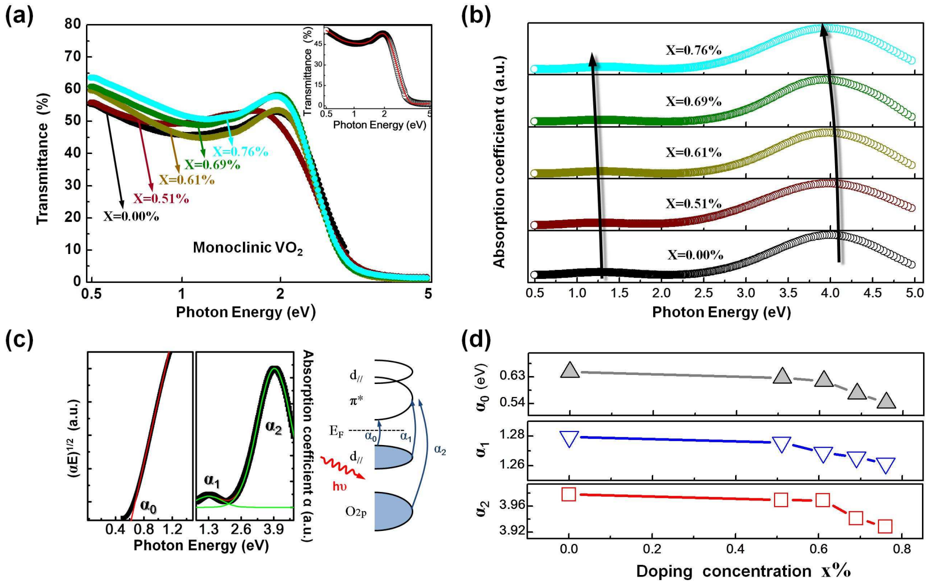

Figure 6. (a) Optical transmittance of $V_{1-x}W_xO_2$ thin films for monoclinic state. Inset shows a typical experimental (circle) and fitting (red line) transmittance spectra with W doping concentration x=0.00%. (b) The relationship of absorption coefficients and photon energy for $V_{1-x}W_xO_2$ with different W doping concentration. (c) Left: $(\alpha E)^{1/2}$ vs the photon energy E is used to determine the optical band gap (OBG) α_0, and absorption spectra in the range from 0.5 to 5.0 eV is used to determine α_1 and α_2 for $V_{1-x}W_xO_2$ thin film with x =0.61%; right: schematic electron transition process for α_0, α_1 and α_2. (d) The changes of α_0, α_1 and α_2 for different W doping concentration.

Fig. 7(a) shows the different W doping concentration affects the orbital structure for monoclinic state. When the W doping concentration increases, lower filled $d_{//}$ orbital energy level exhibits a slight decrease relative to the O 2p orbital, which are schematically shown in Fig. 7(b).

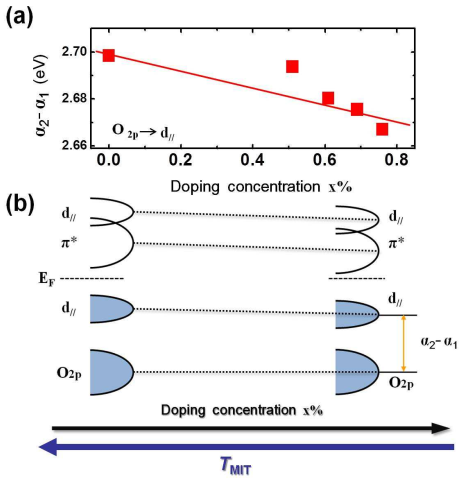

Figure 7. For monoclinic state: (a) α_2-α_1 for different W doping concentration; (b) schematic of the orbital structure change with increasing W doping concentration.

3. 4 Orbital Change Manipulation T_{MIT}

The orbital structure interplay of the rutile and monoclinic states is crucial for modifying the phase transition temperature T_{MIT}. W doping VO_2 can induce significant expansions in its lattice structure, shown in the upper half of Fig. 8(a) (more detailed information can be seen in Fig. 2(d)). Beside, the chemical substitution of V atoms by W atoms with different atom sizes and valence states inevitably drives some additional electrons to accommodate in the π* orbital.[22] Therefore, the combined action of the significant expansion and additional electrons can lead to the orbital structure change of W doping VO_2 thin films.[20,21,22] In Fig. 8(a), we show the orbital structure change with increasing W doping concentration. For rutile state, the relative position change ($\Delta(\pi^*- d_{//})$) of the π* and $d_{//}$ orbital can be given by $\Delta(\beta_2-\beta_1)= (\beta_2-\beta_1)|_x - (\beta_2-\beta_1)|_{x=0}$. The decrease of $\Delta(\pi^*- d_{//})$ indicates that the overlaps of π* orbital and $d_{//}$ orbital increases with increasing W doping content. For monoclinic state, due to the increase of W doping concentration, the relative orbital position change ($\Delta(\pi^*- d_{//})$) of the π^* and lower filled $d_{//}$ orbital decreases with increasing W doping content, which is calculated by $\Delta\alpha_1=\alpha_1|_x-\alpha_1|_{x=0}$. In order to further observe the evolution behavior of the $V_{1-x}W_xO_2$ orbital structure in its phase transition process, temperature-dependent ultraviolet-infrared spectra is also measured. Fig. 8(c) shows a series of absorption coefficients of $V_{1-x}W_xO_2$ sample with x =0.51%, obtained from the temperature-dependent transmission data. The values of β_1 and β_2 have an increase during the $V_{1-x}W_xO_2$ phase transition process, suggesting that the $d_{//}$ and π^* orbital both move to a higher energy level positions relative to the filled O 2p orbital. α_2 also increases in the phase transition process, which indicates that the π^* orbital shifts up relative to the lower filled $d_{//}$ orbital.

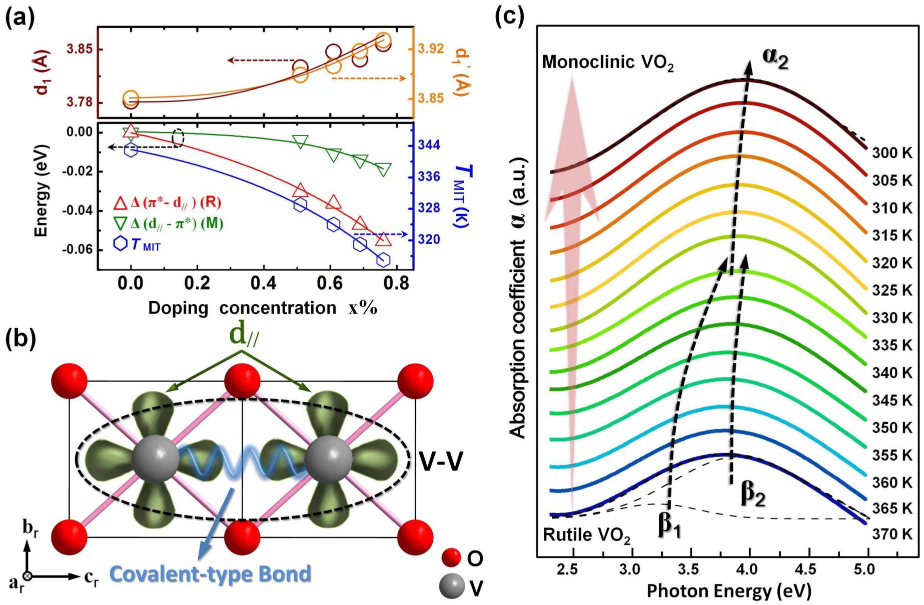

Figure 8. (a) The variation of $\Delta(\pi^*-d_{//})$ for rutile (R) state and $\Delta(d_{//}-\pi^*)$ for monoclinic (M) state corresponding to different W doping concentrations. The changes of average bond lengths (d_1 and d_1') and phase transition temperature T_{MIT} are also shown. Here, lines are guides for eyes. (b)

Owing to the occupation of $d_{//}$ orbital, neighboring V atoms form a covalent-type bond. (c) Absorption coefficient of $V_{1-x}W_xO_2$ sample with x =0.51% at the temperatures range from 300 to 370 K. Dashed lines are guides for the shift of the peaks.

Previous work has focused on understanding the MIT, unfortunately, whether metal–insulator phase transition mechanisms should be described as the Peierls transition, where the dimerization of the V atoms along the rutile c_r axis and consequently opening of the gap, or the Mott transition to a Mott insulating state, where the gap opens due to the strong Coulomb repulsion between the localized V atom 3d orbital and the related dynamical effects, has been a subject of unabated discussions[37,38]. Nevertheless, the basis for above two mechanisms is that a structural change of the VO_6 octahedral modifies local orbital symmetry of the V atoms, which can induce a symmetry breaking to lead a metal-insulator phase transition[37,38,39]. Indeed, Goodenough has pointed out the important role of the V-V pair interactions. In VO_6 octahedron (Fig. 1(a)), because of the occupation of $d_{//}$ orbital, neighboring V atoms can form a covalent-type bond[39,40,41], shown in Fig. 8(b). According to the experimental results in Fig. 8(a), for rutile state, the increase of the overlap between the antibonding π^* and $d_{//}$ orbital can makes the occupancy of $d_{//}$ orbital decrease. Subsequently, some itinerant electrons in the $d_{//}$ orbital can partially transfer to the antibonding π^* orbital. This then reduces the strength of the covalent-type bond. Finally, by changing the occupancy of $d_{//}$ orbital, the phase transition temperature T_{MIT} can be tuned.

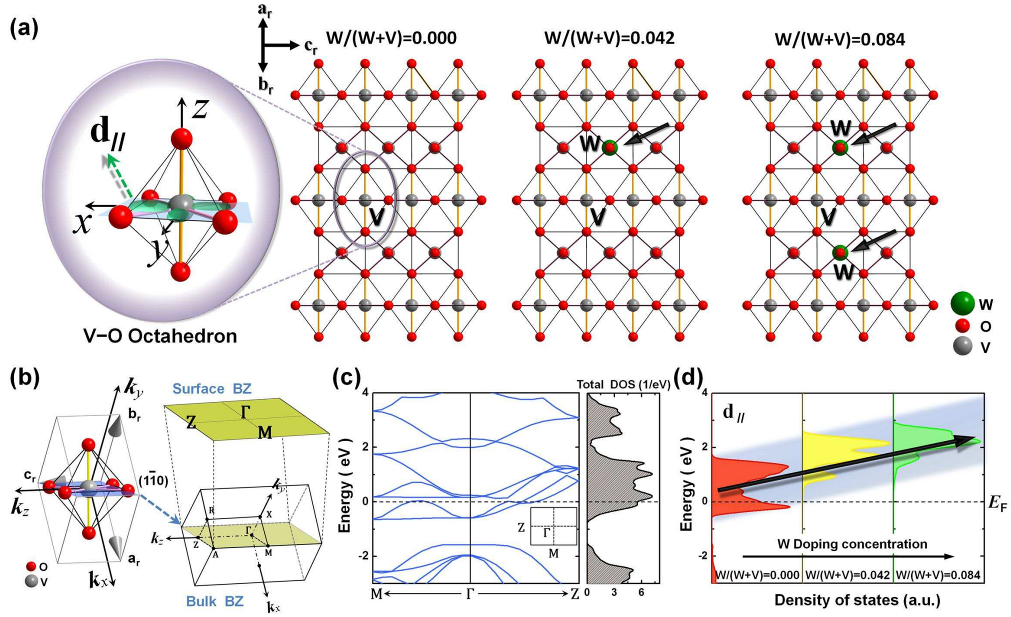

Figure 9. (a) Schematic of W doping VO_2 for rutile states. The left part shows the $d_{//}$ orbital in the V−O octahedral configuration, in which the local coordinate systems of V atom are defined with x axes along c_r direction. (b) Real-space crystal structure and reciprocal-space Brillouin zone (BZ) of rutile VO_2. The $d_{//}$ orbital lies in the $(1\bar{1}0)$ plane (marked by blue) through the origin (Γ) of the bulk Brillouin zone, projecting onto the $(1\bar{1}0)$ surface Brillouin zone (BZ). (c) Band structure along Γ-M and Γ-Z directions with total density of states (DOS) for pure rutile VO_2. (d) The partial density of states (DOS) of corresponding V atom (as marked in (a)) $d_{//}$ orbital for different W doping concentration.

To further confirm the above analysis, we performed first principle calculations. The structures are built from the optimized rutile VO_2 structure. A supercell of 2×2×3 is built to represent pure VO_2 structure. W doping VO_2 is then built from this supercell by replacing V atoms with W atoms. The theoretical calculation is performed using density functional theory (DFT), as implemented in the Vienna *ab initio* Simulation Package (VASP)[42]. The Perdew-Burke-Ernzerhof (PBE) exchange-correlation functional and projector augmented wave pseudopotentials are chosen. The Kohn-Sham wave functions are expanded by plane waves with cut-off energy of 480 eV[43]. The Monkhorst-Pack k points are set to 6×6×6. All the atoms in the supercell are allowed to move and the geometry is relaxed until the forces acting on each atom are less than 0.02 eV/Å. The W/(W+V) atomic ration below 0.042 would require a supercell at least twice larger, which is deemed too demanding for the first principle calculations. Thus, we perform theoretical calculations with three representative W/(W+V) atomic rations: 0.000, 0.042 and 0.084, shown in Fig. 9(a). Fig. 9(b) presents the real-space unit cell and corresponding reciprocal-space Brillouin zone of rutile VO_2. $d_{//}$ orbital investigated in this work lie in the $(1\bar{1}0)$ plane through the origin (Γ) of the bulk Brillouin zone. In Fig. 9(c), the theoretical calculation for pure rutile VO_2 shows the band structure along selected Γ-M and Γ-Z directions. The calculated band structure agrees well with the previous reported results[38]. The partial electron density of states (DOS) for $d_{//}$ orbital with different W doping concentrations is shown in Fig. 9(d). It is clear from Fig. 9(d) that $d_{//}$ orbital is sensitive to the W doping. In Fig. 9(d), the $d_{//}$ orbital of theoretical calculations moves into a higher energy level positions with increasing W doping concentration. β_1 can be assigned to the transition from the filled O 2p orbital to $d_{//}$ orbital. As can be seen in Fig. 4(d), experimental β_1 increases from 3.37 to 3.49 eV with increasing W doping concentration. The experimental results show that $d_{//}$ orbital level position shifts up with increasing W doping concentration, which is consistence with the theoretical calculations.

On the basis of experimental and theoretical results, we can reconstruct a clear physical picture that the $d_{//}$ orbital occupancy can be modulated through controlling the W doping concentration. By decreasing the occupancy of $d_{//}$ orbital, we can reduce the metal-insulator transition temperature T_{MIT}. These results show that the $d_{//}$ orbital occupancy in VO_2 plays an important role on its phase transition process.

4 CONCLUSIONS

In summary, W doping VO_2 films have been prepared by direct-current sputtering deposition. Resistance measurements show that the metal-insulator transition temperature T_{MIT} decreases with increasing W doping content. The orbital structures of $V_{1-x}W_xO_2$ thin films with rutile and monoclinic states have been investigated by ultraviolet-infrared transmittance spectra. Experimental results show that the overlap of π^* and $d_{//}$ orbital for rutile state increases with increasing W doping content. Theoretical calculations also demonstrate that the $d_{//}$ orbital for rutile state shifts to a higher energy level with increasing W doping concentration, which exhibits a good agreement with our experimental measurements. Meanwhile, for monoclinic states, the gap (from the top of lower filled $d_{//}$ orbital to the bottom of empty π^* orbital) decreases with increasing W doping content. These results reveal that the metal-insulator transition temperature T_{MIT} change for W doping VO_2 can come from the $d_{//}$ orbital alteration. Because of the $d_{//}$ orbital occupation, V-V pair can form a covalent-type bonding. With increasing W doping concentration, the decrease of $d_{//}$ orbital occupancy reduces the strength of V-V pair interactions, which finally can lower the transition temperature T_{MIT}. This work provides a direct evidence that the $d_{//}$ orbital change can regulate W doping VO_2 phase transition temperature T_{MIT}.

ACKNOWLEDGEMENTS

The authors are grateful to the supports from the National Natural Science Foundation of China (Grant Nos. 11174049, 61376017, 11174048 and 61376102), the Fundamental Research Funds for the Central Universities and Open Fund of National Laboratory for Infrared Physics, Chinese Academy of Sciences, Shanghai Institute of Technical Physics.

REFERENCES

1. Jaewoo Jeong, NagaphaniAetukuri,TanjaGraf, Thomas D.Schladt, Mahesh G. Samant, Stuart S. P. Parkin. Science, 2013, **339**, 1402-1405.
2. Mengkun Liu, Harold Y. Hwang,HuTao, Andrew C. Strikwerda, Kebin Fan, George R. Keiser, Aaron J. Sternbach,Kevin G. West, Salinporn Kittiwatanakul, Jiwei Lu, Stuart A. Wolf, Fiorenzo G. Omenetto, Xin Zhang, Keith A. Nelson & Richard D. Averitt. Nature, 2012, **487**, 345-348.
3. M. Nakano, K. Shibuya, D. Okuyama, T. Hatano, S. Ono, M. Kawasaki, Y. Iwasa& Y. Tokura. Nature, 2012, **487**, 459-462.
4. E. Arcangeletti,L. Baldassarre,D. Di Castro,S. Lupi,L. Malavasi,C. Marini,A. Perucchi,and P. Postorino. Phys. Rev. Lett., 2007, **98**, 196406.
5. Andrew C. Jones,Samuel Berweger,Jiang Wei,David Cobden and Markus B. Raschke. Nano Lett., 2010, **10**, 1574-1581.

6. D. N. Basov,Richard D. Averitt,Dirk van der Marel ，Martin Dressel and Kristjan Haule.Rev. Mod. Phys., 2011, **83**, 471-541.
7. Myoung-Jae Lee, Youngsoo Park, Dong-Seok Suh, Eun-Hong Lee, Sunae Seo, Dong-Chirl Kim,Ranju Jung, Bo-Soo Kang, Seung-Eon Ahn, Chang Bum Lee, David H. Seo, Young-Kwan Cha,In-Kyeong Yoo, Jin-Soo Kim, and Bae Ho Park. Adv. Mater., 2007, **19**, 3919-3923.
8. Driscoll, Hyun-Tak Kim, Byung-Gyu Chae, Bong-Jun Kim, Yong-Wook Lee, N. Marie Jokerst, S. Palit, D. R. Smith, M. Di Ventra, and D. N. Basov. Science, 2009, **325**, 1518-1521.
9. Jiadong Zhou,Yanfeng Gao, ZongtaoZhang,HongjieLuo,Chuanxiang Cao, Zhang Chen, Lei Dai and Xinling Liu. Sci.Rep., 2013, **3**, 3029.
10. V. Eyert. Phys. Rev. Lett.,2011, **107**, 016401.
11. Nagaphani B. Aetukuri, Alexander X. Gray, Marc Drouard,Matteo Cossale, Li Gao,Alexander H. Reid, Roopali Kukreja, Hendrik Ohldag, Catherine A. Jenkins, Elke Arenholz, Kevin P. Roche, Hermann A. Dürr,Mahesh G. Samant and Stuart S. P. Parkin. Nature Physics, 2013, **9**, 661–666.
12. A. Zylbersztejn and N. F. Mott. Phys. Rev. B, 1975, **11**, 4383.
13. Ran Long, Bingyan Qu, Renchang Tan, Yongfu Sun, Xiaogang Tan, Wu Ying, Bicai Pan,Yujie Xiong and Yi Xi. Phys. Chem. Chem. Phys., 2012, **14**, 7225-7228.

14. Cheng Si, Wei Xu, Huan Wang, Jing Zhou, Abduleziz Ablat, Linjuan Zhang, Jie Cheng, Zhiyun Pan, Lele Fan, Chongwen Zou and Ziyu Wu. Phys. Chem. Chem. Phys., 2012, **14**, 15021–15028.
15. M. Soltani, M. Chaker, E. Haddad, R. V. Kruzelecky, and J. Margot. Appl. Phys. Lett., 2004, **85**, 1958.
16. Dmitry Ruzmetov, Sanjaya D. Senanayake, Venkatesh Narayanamurti, and Shriram Ramanathan. Phys. Rev. B, 2008, **77**,195442.
17. K. Shibuya, M. Kawasaki and Y. Tokura. Appl. Phys. Lett., 2010, **96**, 022102
18. N. R. Mlyuka, G. A. Niklasson and C. G. Granqvist. Appl. Phys. Lett., 2009, **95**, 171909.
19. J. S. Lee,K. Shibuya,M. Kawasaki,and Y. Tokura. Phys. Rev. B, 2012, **85**, 155110.
20. Jamie M. Booth and Philip S. Casey. Phys. Rev. Lett., 2009, **103**, 086402.
21. Xiaogang Tan, Tao Yao, Ran Long, Zhihu Sun, Yajuan Feng, Hao Cheng, Xun Yuan,Wenqing Zhang3, Qinghua Liu, Changzheng Wu, Yi Xie and Shiqiang Wei. Sci.Rep., 2012, **2**, 466.
22. Enju Sakai, Kohei Yoshimatsu, Keisuke Shibuya, Hiroshi Kumigashira, Eiji Ikenaga, Masashi Kawasaki, Yoshinori Tokura, and Masaharu Oshima. Phys. Rev. B, 2011, **84**, 195132.
23. D. Pesquera, G. Herranz, A. Barla, E. Pellegrin, F. Bondino, E. Magnano, F.Sa´nchez and J.Fontcuberta. Nature Communications, 2012, **3**, 1189.

24. Xiaofeng Xu, Anyuan Yin, Xiliang Du, Jiqing Wang, Jiading Liu, Xinfeng He, Xingxing Liu, Yilong Huan. Applied Surface Science, 2010, **256**, 2750-2753.

25. C. Sommers, R. De Groot, D. Kaplan and A. Zylbersztejn. J. Physique Lett., 1975, **36**, 157-160.

26. M. W. Haverkort, Z. Hu, A. Tanaka, W. Reichelt, S. V. Streltsov, M. A. Korotin, V. I. Anisimov, H. H. Hsieh, H.-J. Lin, C. T. Chen, D. I. Khomskii and L. H. Tjeng. Phys. Rev. Lett., 2005, **95**, 196404.

27. Jan M. Tomczak and Silke Biermann. Phys. Rev. B, 2009, **80**, 085117.

28. A. V. Boris, N. N. Kovaleva, S. S. A. Seo, J. S. Kim, P. Popovich, Y. Matiks, R. K. Kremer and B. Keimer. Phys. Rev. Lett., 2009, **102**, 027001.

29. W. Burkhardt, T. Christmann, B.K. Meyer, W. Niessner, D. Schalch, A. Scharmann.Thin Solid Films,1999, **345**, 229-235.

30. W. W. Li, Q. Yu, J. R. Liang, K. Jiang, Z. G. Hu, J. Liu, H. D. Chen and J. H. Chu. Appl. Phys. Lett. 2011, **99**, 241903.

31. Xiaoxiang Xi, Y. M. Dai, C. C. Homes, M. Kidszun, S. Haindl, and G. L. Carr. Phys. Rev. B, 2013, **87**, 180509.

32. A. Charnukha, D. Pröpper, T. I. Larkin, D. L. Sun, Z. W. Li, C. T. Lin, T. Wolf, B. Keimer, and A. V. Boris. Phys. Rev. B, 2013, **88**, 184511.

33. Peter Uhd Jepsen, Bernd M. Fischer, Andreas Thoman, Hanspeter Helm, J. Y. Suh, René Lopez, and R. F. Haglund, Jr. Phys. Rev. B, 2006, **74**, 20510.

34. Max Born and Emil Wolf. Principles of Optics. 7th Revised edition (Cambridge University Press, 1999).

35. R J O Mossanek and M Abbate. J. Phys.: Condens. Matter, 2007, **19**, 346225.

36. A. Continenza, S. Massidda and M. Posternak. Phys. Rev. B,1999, **60**, 15699.

37. Peter Baum, Ding-Shyue Yang, Ahmed H. Zewail. Science, 2007, **318**, 788-792.

38. M. M. Qazilbash, M. Brehm, Byung-Gyu Chae, P.-C. Ho1, G. O. Andreev, Bong-Jun Kim, Sun Jin Yun, A. V. Balatsky, M. B. Maple, F. Keilmann, Hyun-Tak Kim, D. N. Basov. Science, 2007, **318**, 1750-1753.

39. Takashi Mizokawa. Nature Physics, 2013, **9**, 612-613.

40. Goodenough, J. B. J. Solid State. Chem., 1971, **3**, 490-500.

41. Volker Eyert. Ann. Phys. (Leipzig), 2002, **11**, 650-702.

42. Shuanglin Hu ,S.-Y. Li ,R. Ahuja,C. G. Granqvist,K. Hermansson,G. A. Niklasson and R. H. Scheicher. Appl. Phys. Lett., 2012, **101**, 201902.

43. J. P. Perdew, K. Burke, and M. Ernzerhof, Phys. Rev. Lett.,1996, **77**, 3865.